nature nanotechnology

LETTERS

https://doi.org/10.1038/s41565-019-0405-2

# Probing van der Waals interactions at two-dimensional heterointerfaces

Baowen Li[1,2], Jun Yin[1,2], Xiaofei Liu[1,2], Hongrong Wu[1], Jidong Li[1], Xuemei Li[1] and Wanlin Guo[1*]

**Two-dimensional (2D) heterostructures assembled via van der Waals (vdW) interactions have sparked immense interest in fields from physics[1,2] to electronics[3,4]. Understanding the vdW interaction at these heterointerfaces is critical for the sophisticated construction and manipulation of these 2D heterostructures. However, previous experimental research has mainly focused on the interlayer interactions in homogeneous graphite crystals[5,6] and the interactions between graphene and substrates[7]. Theoretically, although a variety of vdW methods have been incorporated in density functional theory to probe the interactions of homogeneous vdW crystals, the reliability of these vdW methods in 2D heterostructures remains to be verified. Here, we show, by contact-splitting transfer of graphite from hexagonal boron nitride (BN) to molybdenum disulfide ($MoS_2$), that graphite experiences a stronger vdW interaction with $MoS_2$ than with boron nitride. Quantitative measurements using a graphite-wrapped atomic force microscope tip show that the critical adhesion pressures between BN and graphite and $MoS_2$ and graphite are respectively 0.953 and 1.028 times that between graphite and graphite. The results are consistent with the prediction based on Lifshitz theory, implying an important role of material dielectric function in the vdW interactions at heterointerfaces. These findings offer us more freedom in the construction of 2D heterostructures, and a technique to disassemble 2D heterostructures is demonstrated.**

Van der Waals interactions in 2D heterostructures were investigated experimentally using two different strategies, quantitative measurements of the critical adhesion force at the nanoscale using an atomic force microscope (AFM) with a graphite-wrapped tip and qualitative comparison through contact-splitting tests at the microscale. Graphite, hexagonal BN and $MoS_2$ are chosen as three typical 2D materials with very different electrical properties to probe the vdW interactions at heterointerfaces. For conciseness, we mainly focus on the graphite–BN and graphite–$MoS_2$ interfaces in this work. Although the monolayers of these vdW crystals are all in the form of a hexagonal lattice (Fig. 1a), $MoS_2$ consists of two surface sulfur layers and one interior molybdenum layer, unlike the single-atomic thin graphene and BN. The surface density of the top sulfur atoms of the $MoS_2$ in direct contact with neighbouring material is ~10 atoms $nm^{-2}$, which is ~3.2 times sparser than that of BN and graphite. Simply assuming the validity of the proportional relationship between the vdW interaction and surface atom density and ignoring the element difference will lead to an intuitive judgement that the critical adhesion force between $MoS_2$ and graphite should be significantly lower than that of BN and graphite, but this is not the case, as described in the following.

AFM has shown its versatility in probing the mechanical properties of systems from nanomaterials to biological samples. To elucidate the vdW interactions between different 2D materials, a silicon AFM tip was wrapped with a thin graphite flake of thickness ~10 nm, as schematically illustrated in Fig. 1b. The wrapping process was carefully designed and conducted to prevent possible contamination on top of the graphite surface (see Supplementary Information for details and Supplementary Fig. 1a). Force–distance curves were measured in high vacuum ($1 \times 10^{-7}$ torr) at room temperature (~25 °C) to eliminate contributions from water capillary action between the tip and flake. The BN and $MoS_2$ flake were aligned on top of the graphite flake (Supplementary Fig. 2c), enabling the characterization of all three materials on the same sample. Before measuring the force–distance curves, the AFM tip was brought into contact with the substrate, which was then annealed in situ at 200 °C to remove the airborne hydrocarbon adsorbed on both substrates and graphite tip[8].

Typical force–distance curves for the three substrates are shown in Fig. 1c. In the approach stage (wine-coloured arrow), the tip first jumped to contact the substrate once the gradient of the attractive force exceeded the probe cantilever stiffness, and then was further pushed towards the substrate with a linear increase in the applied force. During retraction (red arrow), the applied force was released linearly and became negative until the elastic force of the cantilever exceeded the critical adhesion force, where the tip jumped from contact. The discrepancy in the slopes of the approach and retraction lines is attributed to the hysteresis effect of the piezoelectric scanning stage. Once the contact area between the tip and substrate is known, the critical adhesion force between the graphite and BN or $MoS_2$ could be directly deduced.

Unfortunately, it is always challenging to precisely determine the contact area between a AFM tip and a substrate, especially with the graphite-wrapped AFM tip, where the graphite flake has to crumple to conform to the tip shape (Supplementary Fig. 2b). We therefore measured the critical adhesion forces between different pairs of materials, that is, graphite–graphite ($P_{G/G}$), graphite–BN ($P_{BN/G}$) and graphite–$MoS_2$ ($P_{MoS2/G}$), using the same tip. The critical adhesion pressures between graphite–BN and graphite–$MoS_2$ were then deduced from their ratios to the pressure between incommensurate graphite–graphite, which has been determined to be $1.1 \pm 0.15$ GPa (refs. [9–11]). The stability of the measured adhesion force during 100 measurements (Supplementary Figs. 3 and 4) indicates that there is no systemic change of the contact area during the measurements, and the statistical results for $P_{G/G}$ are shown in Fig. 1d. Histograms $P_{BN/G}/P_{G/G}$ and $P_{MoS2/G}/P_{G/G}$ are presented in Fig. 1e, and it is clear that $P_{BN/G}$ is lower than $P_{MoS2/G}$. Based on the determined ratios, the critical adhesion pressures for graphite–BN and graphite–$MoS_2$ are deduced to be $1.049 \pm 0.013$ GPa and $1.131 \pm 0.014$ GPa, respectively.

[1]Key Laboratory for Intelligent Nano Materials and Devices of the Ministry of Education, State Key Laboratory of Mechanics and Control of Mechanical Structures, Institute of Nanoscience of Nanjing University of Aeronautics and Astronautics, Nanjing, China. [2]These authors contributed equally: Baowen Li, Jun Yin, Xiaofei Liu. *e-mail: wlguo@nuaa.edu.cn

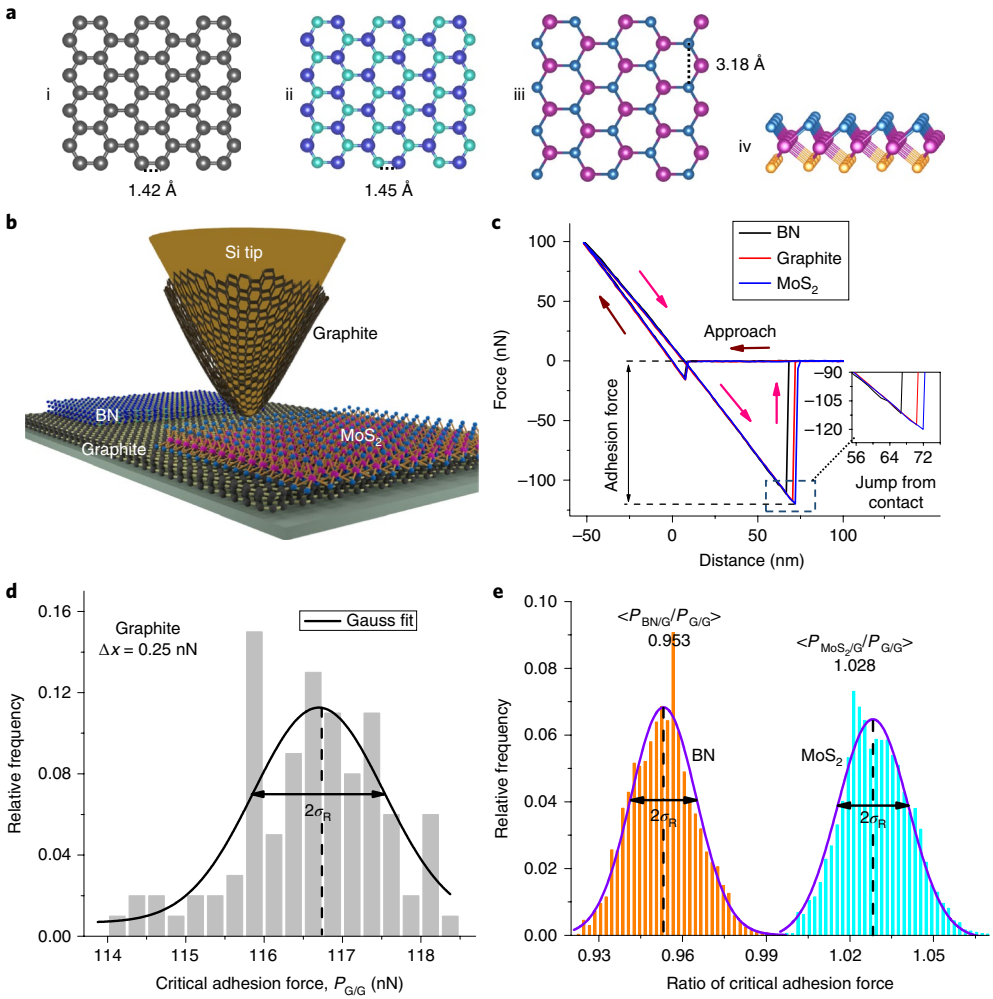


**Fig. 1 | Critical adhesion force between 2D materials measured by an atomic force microscope. a**, Lattice constant and surface atoms of graphite (i), BN (ii) and $MoS_2$ (iii, iv), where the top- and bottom-layer sulfur atoms in $MoS_2$ are shown in blue and yellow, respectively. **b**, Schematic illustration of an AFM tip wrapped with a thin graphite layer in contact with BN–$MoS_2$/graphite. **c**, Typical force–distance curves measured on BN, $MoS_2$ and graphite, respectively. Inset, Enlarged view of the critical adhesion force. **d**, Histogram distribution of graphite–graphite critical adhesion force $P_{G/G}$ determined in 100 measurements. The black line is a Gaussian fit with a sampling interval of $\Delta x = 0.25$ nN. **e**, Histogram distribution of the ratio of measured critical adhesion forces in graphite–BN ($P_{BN/G}$) and graphite–$MoS_2$ ($P_{MoS2/G}$) to that in graphite–graphite ($P_{G/G}$), respectively. A total of 100 measurements were performed on each pair. Instead of obtaining the $P_{BN/G}/P_{G/G}$ ratio by dividing the $P_{BN/G}$ by the mean of $P_{G/G}$, 10,000 values of the $P_{BN/G}/P_{G/G}$ ratio were calculated by dividing every measured $P_{BN/G}$ value by every measured $P_{G/G}$ and using this for the fitting. In this way, the deviation in the $P_{G/G}$ data fitting is preserved. The same method was applied to obtain the $P_{MoS2/G}/P_{G/G}$ ratio. The data were recorded at a sampling interval of $\Delta x = 0.002$, and Gaussian fits (violet line) provide $P_{MoS2/G}/P_{G/G} = 1.028 \pm 0.013$ and $P_{BN/G}/P_{G/G} = 0.953 \pm 0.012$. $\sigma_R$ in **d** and **e** means the standard deviation in the Gaussian fits.

In the AFM measurements, the relative crystalline orientations between the graphite tip and substrates are random. To investigate if the results are dependent on stacking orientations, we developed a microscale contact-splitting competition strategy to compare their interlayer interaction qualitatively. As illustrated in Fig. 2a, the contact-splitting test consists of three steps. First, two flexible polymer substrates were used to separately pick up large BN and $MoS_2$ flakes (thickness ~50–70 nm). One of the flake/polymer substrates was then used to pick up a small graphite flake of thickness ~5–15 nm (left panel of Fig. 2a). The 50–70 nm thickness of the BN and $MoS_2$ flakes ensures that the vdW contribution from the polymers can be ignored. During the pick-up process, the relative angle between the straight edges of two flakes was adjusted to the desired values within an error of 2°. Because the edges of all three materials prefer to be along the zigzag/armchair orientations, the stacking orientations between them can be feasibly controlled in this way[12]. The pick-up process was conducted at around 90 °C to prevent the accumulation of trapped contamination between two flakes, as evidenced by the absence of trapped bubbles between the stacked flakes (Supplementary Fig. 5). The self-cleansing process spontaneously taking place at their interfaces guarantees the atomically clean interface[13] required for investigation of the vdW interaction. The two polymer substrates were then pushed towards each other until the graphite flake was totally encapsulated by BN and $MoS_2$, but with the BN and $MoS_2$ still partially separated (middle panel of Fig. 2a). During this process, the straight edges of the BN and $MoS_2$ were also aligned parallel to ensure that they had the same stacking orientation to the graphite. Finally, the BN–graphite–$MoS_2$ stack was split along the BN–$MoS_2$ interface, and optical images were taken to check to which material the graphite flake was stuck.

As shown in Fig. 2b, all of the graphite flakes were transferred from BN onto $MoS_2$ flakes after the contact-splitting tests,

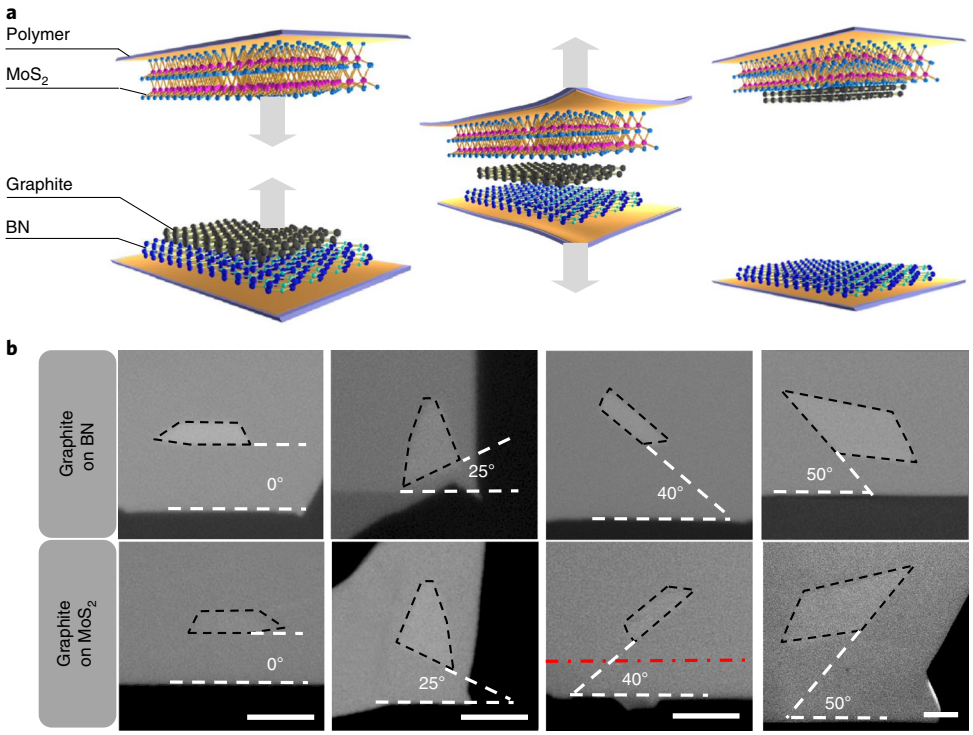


**Fig. 2 | Contact-splitting competition test of BN–graphite–$MoS_2$. a**, Schematic illustration of the contact-splitting competition test. A graphite–BN stack and $MoS_2$ flake (or graphite–$MoS_2$ and BN) were first prepared on flexible polymer substrates (left) and then put into contact with each other until the graphite was fully encapsulated (middle). Finally, the BN–graphite–$MoS_2$ stack was split along the $MoS_2$–BN interface to see to which material the graphite flake preferred to stick (right). **b**, Optical images of the results for BN–graphite–$MoS_2$ stacks of different stacking orientations. Scale bars, 5 μm. The red dashed-dotted line in the bottom panel marks the position where the top and bottom sections of the original micrograph are stitched together while a middle section is removed, and the edges of graphite and $MoS_2$ flakes shown in the figure are brought closer without relative rotation.

regardless of the stacking orientation (0°, 25°, 40° or 50°). When we performed inverse contact-splitting process by first picking up graphite using $MoS_2$, the graphite flake never transferred from $MoS_2$ to BN. During the contact-splitting test, all the other factors remain the same except for $MoS_2$ and BN flake which are in direct contact with graphite; thus it is reasonable to infer that it is the vdW interaction at the graphite–BN and graphite–$MoS_2$ interfaces that determines to which materials graphite prefers to adhere. The results of contact-splitting tests also indicate a stronger vdW interaction at the graphite–$MoS_2$ interface compared with graphite–BN interface regardless of the relative crystalline orientations, which is consistent with the AFM measurements. The orientation independence is further confirmed by the contact-splitting test with random flake orientations (Supplementary Fig. 6).

To understand the experimental results, we performed density functional theory (DFT) calculations using the Perdew–Burke–Ernzernhof (PBE) exchange-correlation functional[14]. Because the PBE functional lacks the long-range vdW interactions, five DFT-based vdW methods were applied: (1) many-body-dispersion methods[15], (2) Grimme's DFT+D2[16], (3) vdW-DF[17], (4) the non-local vdW functionals OPT88[18] and (5) Tkatchenko and Scheffler's (TS) vdW method[19]. These methods have been widely applied in molecular crystals[20], solid materials[21], metal–organic frameworks[22,23] and biomolecules[24], and have been benchmarked in homogeneous vdW crystals with experimental results or random phase approximation calculations[25]. In the calculations, we simulated the heterostructures using stacked monolayer crystals instead of flakes of experimental thickness due to limitations in computational resources. Although the thicknesses of the flakes do affect the calculated vdW energy, the qualitative conclusion does not depend on it, as discussed in the Methods.

Figure 3a show the interlayer binding energy as a function of displacement away from the corresponding equilibrium positions for the graphene–BN and graphene–$MoS_2$ heterostructures, respectively. It can be seen that, once the long-range dispersion interactions are included, the binding energies become negative at the equilibrium positions and converge to zero at infinitely large displacement. The equilibrium distance $d_0$, binding energy $E_b$ and critical adhesion force $P_c$ calculated by the five vdW methods are listed in Supplementary Table 1. In general, all the vdW models predict a stronger binding energy in the graphene–BN interface, except for the vdW-DF method, which leads to quite close binding energies. With respect to the critical adhesion force that dominates the splitting process, all the methods predict a higher $P_c$ in graphene–BN (Fig. 3b), which is in conflict with the experimental results. According to test simulations, this inconsistency cannot be attributed to the presence of the sulfur vacancies usually observed in $MoS_2$. The pairwise vdW methods using vdW coefficients and atomic polarizabilities derived from free atoms ignore the effect of covalent bonding and dipole–dipole screening on material dielectric functions, which might be the reasons for the inconsistencies with experiment.

To find a theoretical vision that can distinguish the difference in the vdW interactions at the 2D heterointerfaces, we calculated the interlayer vdW energies from the dielectric functions of the vdW crystals. According to Lifshitz theory (LZ)[26,27], the vdW energy was calculated as the difference between the free energy of electromagnetic modes propagating between two dielectric slabs (as illustrated in Fig. 4a) and the free energy in two isolated slabs. The frequency-dependent dielectric functions obtained from random phase approximation[28] (Fig. 4b) were used to calculate the allowed electromagnetic modes, thus taking into account the effect of

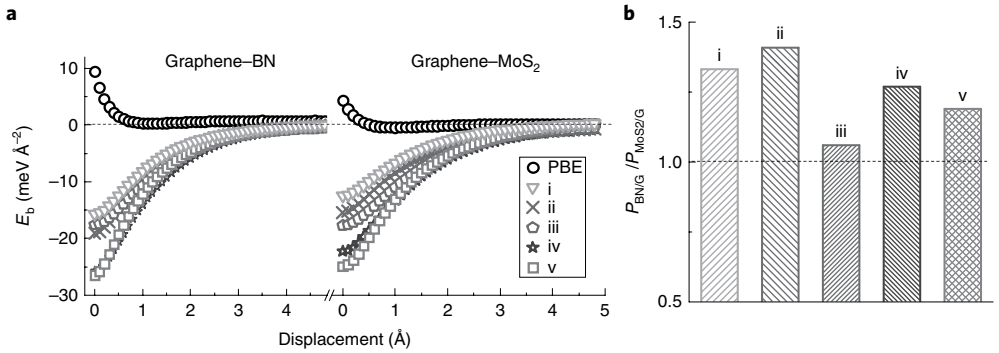


**Fig. 3 | Interlayer interactions calculated by DFT-based vdW methods. a**, Binding energies as a function of interlayer displacement from corresponding equilibrium positions in graphene–BN and graphene–$MoS_2$ heterostructures. The zero displacement in PBE is set to that in PBE+D2. **b**, Critical force ratio of graphene–BN to graphene–$MoS_2$ deduced from DFT calculations: (i) many-body dispersion methods; (ii) Grimme's DFT+D2, (iii) vdW-DF, (iv) the non-local vdW functionals OPT88 and (v) Tkatchenko and Scheffler's vdW method.

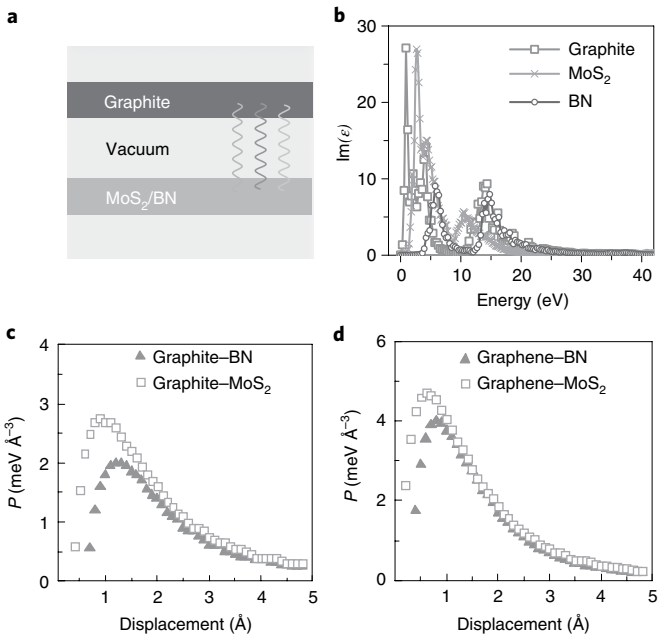


**Fig. 4 | Interlayer force derived from Lifshitz theory. a**, Illustration of the model used in Lifshitz theory. **b**, Imaginary dielectric function of the bulk vdW crystals calculated using the random phase approximation. The real part of the dielectric function was derived from the imaginary part according to the Kramers–Kronig relation. **c**, Force as a function of inter-slab displacement for 5 nm graphite–5 nm BN and for 5 nm graphite–5 nm $MoS_2$. The equilibrium positions of PBE+D2 are taken as the zero displacement. The surface thicknesses of the electron clouds of the bulk slabs are set at 0.5 Å. The total energy includes both the PBE electrostatic energy and the LZ vdW energies. **d**, Force per unit area as a function of interlayer displacement for graphene–BN and graphene–$MoS_2$ heterogeneous bilayers. The surface thicknesses of monolayer graphene, BN and $MoS_2$ are set as 0.77, 0.82 and 0.68 Å, respectively.

covalent bonding and dipole–dipole screening on vdW energy. Figure 4c shows the PBE+LZ interfacial forces as a function of vertical displacement for 5 nm slabs of graphite, BN and $MoS_2$. Consistent with our experiments, the PBE+LZ critical force in the graphite–$MoS_2$ heterointerface is higher. This is understandable as $MoS_2$ having higher imaginary dielectric constants than BN, especially in the low-frequency region. Meanwhile, the weaker PBE electrostatic repulsion in the graphite–$MoS_2$ heterointerface (Fig. 3a) also contributes to its stronger binding. Figure 4d shows the PBE+LZ interfacial forces in the heterogeneous bilayers, showing the same relative strength of the vdW interaction. It is worth noting that the critical adhesion forces for the monolayers are higher than those of thicker slabs, which should be common for all vdW crystals, because the vdW energy as a function of distance for the monolayers complies with a power law relation different from that for the bulk[29]. The agreement between the LZ model and our experiment implies an important role of material dielectric function in determining the vdW interactions in heterointerfaces. To further verify this implication, contact-splitting tests were conducted for BN–graphite–$MoSe_2$ (Supplementary Fig. 7). As expected, graphite prefers to stick to $MoSe_2$ instead of BN, as the dielectric constant of $MoSe_2$ is comparable to that of $MoS_2$(ref. [30]) and higher than that of BN.

Our additional experiments show that $MoS_2$ not only wins the competition with BN to attract graphite, but also exerts a stronger attraction to BN compared with graphite (Supplementary Fig. 8). Based on these results, we demonstrated that a graphite–BN–graphite heterostructure can be disassembled flake by flake using $MoS_2$ as a manipulator, as shown in Fig. 5. The most important thing here is that, after these manipulations, the surfaces of these 2D materials are still atomic clean without introduced defects and contaminations. The technique demonstrated here offers us broader space to manipulate the 2D heterostructures and probe their extraordinary properties.

## Conclusion

The vdW interactions at graphite–graphite, graphite–$MoS_2$ and graphite–BN interfaces are systematically investigated through AFM measurements using a graphite-wrapped AFM tip and a contact-splitting competition experiment. It is revealed that $MoS_2$ always experiences a stronger attraction to graphite compared with BN regardless of their relative stacking orientations. Quantitative measurements show that $P_{BN/G}$ and $P_{MoS2/G}$ are 0.953 and 1.028 times $P_{G/G}$, respectively. Lifshitz theory, which takes the material dielectric function into account, can rationalize the interactive forces at the heterointerfaces, but five commonly used DFT-based vdW models, which are mainly benchmarked for homogeneous interfaces, cannot describe the experimental results. These results imply that the material dielectric function plays an important role in determining the vdW interactions at the heterointerfaces, which is further checked by comparing the strength of interaction at the graphite–$MoSe_2$ and graphite–BN heterointerfaces. Based on these results, a technique to disassemble 2D heterostructures has been developed and demonstrated, offering us more freedom in the construction of 2D heterostructures and their applications.

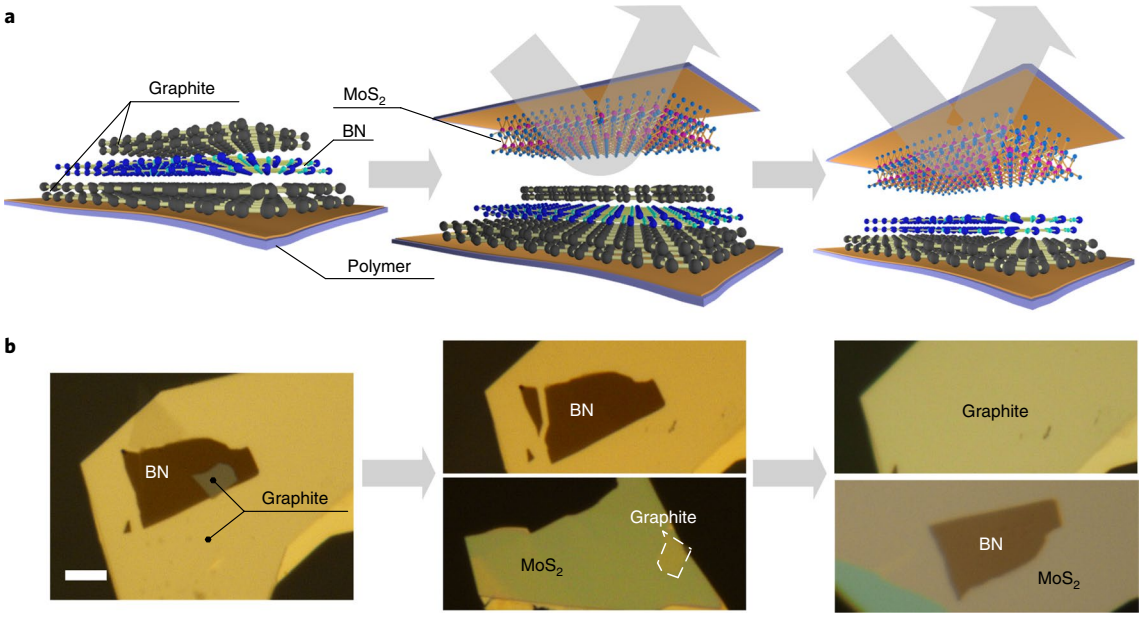


**Fig. 5 | Disassembling the graphite–BN–graphite heterostructure, flake by flake, using $MoS_2$ as a manipulator. a**, Schematic illustration of the disassembly process. **b**, Optical images of the original graphite–BN–graphite stack (left), whose top graphite was first removed (middle) followed by removal of the BN flake (right). Scale bar, 5 μm.

## Online content

Any methods, additional references, Nature Research reporting summaries, source data, statements of data availability and associated accession codes are available at https://doi.org/10.1038/s41565-019-0405-2.

Received: 29 January 2018; Accepted: 12 February 2019;
Published online: 25 March 2019

## References

1. Dean, C. et al. Hofstadter's butterfly and the fractal quantum Hall effect in moire superlattices. *Nature* **497**, 598–602 (2013).
2. Kumar, R. K. et al. High-temperature quantum oscillations caused by recurring Bloch states in graphene superlattices. *Science* **357**, 181–184 (2017).
3. Liu, Y. et al. Van der Waals heterostructures and devices. *Nat. Rev. Mater.* **1**, 16042 (2016).
4. Chen, S. et al. Electron optics with pn junctions in ballistic graphene. *Science* **353**, 1522–1525 (2016).
5. Liu, Z. et al. Interlayer binding energy of graphite: a mesoscopic determination from deformation. *Phys. Rev. B* **85**, 205418 (2012).
6. Koren, E., Lörtscher, E., Rawlings, C., Knoll, A. W. & Duerig, U. Adhesion and friction in mesoscopic graphite contacts. *Science* **348**, 679–683 (2015).
7. Koenig, S. P., Boddeti, N. G., Dunn, M. L. & Bunch, J. S. Ultrastrong adhesion of graphene membranes. *Nat. Nanotechnol.* **6**, 543–546 (2011).
8. Ishigami, M., Chen, J., Cullen, W., Fuhrer, M. & Williams, E. Atomic structure of graphene on $SiO_2$. *Nano Lett.* **7**, 1643–1648 (2007).
9. Wang, W. et al. Measurement of the cleavage energy of graphite. *Nat. Commun.* **6**, 7853 (2015).
10. Cuenot, S., Fretigny, C., Demoustier-Champagne, S. & Nysten, B. Surface tension effect on the mechanical properties of nanomaterials measured by atomic force microscopy. *Phys. Rev. B* **69**, 165410 (2004).
11. Gould, T. et al. Binding and interlayer force in the near-contact region of two graphite slabs: experiment and theory. *J. Chem. Phys.* **139**, 224704 (2013).
12. You, Y., Ni, Z., Yu, T. & Shen, Z. Edge chirality determination of graphene by Raman spectroscopy. *Appl. Phys. Lett.* **93**, 163112 (2008).
13. Pizzocchero, F. et al. The hot pick-up technique for batch assembly of van der Waals heterostructures. *Nat. Commun.* **7**, 11894 (2016).
14. Perdew, J. P., Burke, K. & Ernzerhof, M. Generalized gradient approximation made simple. *Phys. Rev. Lett.* **77**, 3865 (1996).
15. Tkatchenko, A., DiStasio, R. A. Jr, Car, R. & Scheffler, M. Accurate and efficient method for many-body van der Waals interactions. *Phys. Rev. Lett.* **108**, 236402 (2012).
16. Grimme, S., Antony, J., Ehrlich, S. & Krieg, H. A consistent and accurate ab initio parametrization of density functional dispersion correction (DFT-D) for the 94 elements H–Pu. *J. Chem. Phys.* **132**, 154104 (2010).
17. Dion, M., Rydberg, H., Schröder, E., Langreth, D. C. & Lundqvist, B. I. Van der Waals density functional for general geometries. *Phys. Rev. Lett.* **92**, 246401 (2004).
18. Klimeš, J., Bowler, D. R. & Michaelides, A. Chemical accuracy for the van der Waals density functional. *J. Phys. Condens. Matter* **22**, 022201 (2009).
19. Tkatchenko, A. & Scheffler, M. Accurate molecular van der Waals interactions from ground-state electron density and free-atom reference data. *Phys. Rev. Lett.* **102**, 073005 (2009).
20. Marom, N. et al. Many-body dispersion interactions in molecular crystal polymorphism. *Angew. Chem. Int. Ed.* **52**, 6629–6632 (2013).
21. Gao, W. & Tkatchenko, A. Electronic structure and van der Waals interactions in the stability and mobility of point defects in semiconductors. *Phys. Rev. Lett.* **111**, 045501 (2013).
22. Liu, X., Hermann, J. & Tkatchenko, A. Communication: many-body stabilization of non-covalent interactions. Structure, stability, and mechanics of $Ag_3Co(CN)_6$ framework. *J. Chem. Phys.* **145**, 241101 (2016).
23. Sapnik, A. et al. Uniaxial negative thermal expansion and metallophilicity in $Cu_3[Co(CN)_6]$. *J. Solid State Chem.* **258**, 298–306 (2018).
24. Tkatchenko, A., Rossi, M., Blum, V., Ireta, J. & Scheffler, M. Unraveling the stability of polypeptide helices: critical role of van der Waals interactions. *Phys. Rev. Lett.* **106**, 118102 (2011).
25. Björkman, T., Gulans, A., Krasheninnikov, A. & Nieminen, R. Are we van der Waals ready? *J. Phys. Condens. Matter* **24**, 424218 (2012).
26. Sarabadani, J., Naji, A., Asgari, R. & Podgornik, R. Many-body effects in the van der Waals–Casimir interaction between graphene layers. *Phys. Rev. B* **84**, 155407 (2011).
27. Lifshitz, E. The theory of molecular attractive forces between solids. *Sov. Phys. JETP* **2**, 73–83 (1956).
28. Harl, J. & Kresse, G. Cohesive energy curves for noble gas solids calculated by adiabatic connection fluctuation-dissipation theory. *Phys. Rev. B* **77**, 045136 (2008).
29. Parsegian, V. A. in *Van der Waals Forces: A Handbook for Biologists, Chemists, Engineers, and Physicists* Ch. 2 (Cambridge Univ. Press, 2005).
30. Kumar, A. & Ahluwalia, P. K. Tunable dielectric response of transition metals dichalcogenides $MX_2$ (M = Mo, W; X = S, Se, Te): effect of quantum confinement. *Physica B Phys. Condens. Matter* **407**, 4627–4634 (2012).

## Acknowledgements

This work was supported by the NSF of China (grants nos. 51535005, 11702132, 51472117 and 51702159) and NSF of Jiangsu Province (grants nos. BK20170770 and BK20170791). The authors also acknowledge support from the China Postdoctoral Science Foundation (grants nos. 2016M600408, 2017T100362 and 2017M610328),

Jiangsu Postdoctoral Research Funds (no. 1701141B), the Fundamental Research Funds for the Central Universities (no. NC2018001) and a project funded by the Priority Academic Program Development of Jiangsu Higher Education Institutions.

## Author contributions

W.G., J.Y. and B.L. designed the experimental strategy. B.L., J.Y. and H.W. performed the experiments. X. Liu designed and performed the theoretical study. All authors contributed to the analysis and discussion. W.G., B.L., J.Y. and X. Liu wrote the manuscript.

## Competing interests

The authors declare no competing interests.

## Additional information

**Supplementary information** is available for this paper at https://doi.org/10.1038/s41565-019-0405-2.

**Reprints and permissions information** is available at www.nature.com/reprints.

**Correspondence and requests for materials** should be addressed to W.G.

**Journal peer review information** *Nature Nanotechnology* thanks José María Gomez-Rodriguez, Kian Ping Loh and other anonymous reviewer(s) for their contribution to the peer review of this work.